PHYSICAL REVIEW B **99**, 245149 (2019)

All-electron product basis set: Application to plasmon anisotropy in simple metals

J. A. Budagosky[1] and E. E. Krasovskii[1,2,3]

[1]*Donostia International Physics Center (DIPC), Paseo Manuel de Lardizabal 4, 20018 Donostia/San Sebastián, Basque Country, Spain*
[2]*Departamento de Física de Materiales, Facultad de Ciencias Quíimicas, Universidad del Pais Vasco/Euskal Herriko Unibertsitatea, Apdo. 1072, 20080 Donostia/San Sebastián, Basque Country, Spain*
[3]*IKERBASQUE, Basque Foundation for Science, 48013 Bilbao, Basque Country, Spain*

(Received 26 February 2019; revised manuscript received 14 May 2019; published 26 June 2019)

An efficient basis set for products of all-electron wave functions is proposed, which comprises plane waves defined over the entire unit cell and orbitals confined to small nonoverlapping spheres. The size of the set and the basis functions are, in principle, independent of the computational parameters of the band-structure method. The approach is implemented in the extended linearized augmented plane wave method, and its properties and accuracy are discussed. The method is applied to analyze the dielectric response of the simple metals Al, Na, Li, K, Rb, and Cs with a focus on the origin of the anisotropy of the plasmon dispersion in Al and Na. The anisotropy is traced to tiny structures of the one-particle excitation spectra of Al and Na, and relevant experimental observations are explained.

DOI: 10.1103/PhysRevB.99.245149

I. INTRODUCTION

The microscopic dielectric function (DF) $\epsilon(\mathbf{r},\mathbf{r}';\omega)$ is a key ingredient in the theory of the ground state [1], quasiparticles [2,3], optical [4], and plasmonic [5–8] excitations as well as in the electron spectroscopies where the microscopic electric field in the solid is a crucial aspect: photoemission at low photon energies [9], laser-assisted time-resolved spectroscopy [10], or the theory of energy losses by quantum particles [11]. The variety of applications and the growing demand for a detailed description of the DF calls for the development of an efficient basis set to express the relevant operators in order to facilitate *ab initio* calculations of the DF.

A general and rigorous analysis of the basis set problem was presented by Harriman [12], and various practical schemes have been implemented. The simplest case are pseudopotential methods [13,14], where the plane-wave (PW) basis for the Bloch wave functions $\psi_\lambda^{\mathbf{k}}$ is ideally suited for the Fourier representation of the dielectric matrix $\epsilon_{\mathbf{GG}'}(\mathbf{q},\omega)$, which immediately follows from the Fourier expansion of the products $\psi_{\lambda'}^{\mathbf{k}*}\psi_\lambda^{\mathbf{k}-\mathbf{q}}$. Furthermore, the accuracy of both $\psi_\lambda^{\mathbf{k}}$ and $\epsilon(\mathbf{r},\mathbf{r}';\omega)$ is consistently controlled by a cutoff in the reciprocal space. Another obvious choice is a real-space grid [15,16]; however, the experience with the projected augmented wave method shows that atomic-orbital basis is computationally more efficient [17]. Typical implementation of the orbital basis in the context of pseudopotentials and accompanying approximations are discussed in Refs. [18,19]. The problem becomes nontrivial in all-electron methods, where the basis functions have complicated shapes, and their products are unwieldy. In addition, the resulting product set is nonorthogonal and overcomplete, and there is no *a priori* criterion to reduce the set and to control its convergence. For orbital basis sets, methods of numerical elimination of redundant products were suggested by Aryasetiawan and Gunnarsson [20] for muffin-tin orbitals and by Foerster [21] for atomic orbitals. The most accurate wave functions are provided by the augmented plane wave (APW) formalism, where the basis functions are still more complicated [22–26]. In the LAPW-based (linear APW) codes [27–29], criteria similar to those of Refs. [20,21] are applied to obtain a reduced set from the products of APWs. However, no attempt has been made to construct a universal basis to parametrize the products.

Here, we propose a basis set to calculate the ϵ matrix out of all-electron wave functions, which is suitable for (but not limited to) the APW representation. The product basis set consists of plane waves that are defined throughout the unit cell (not just in the interstitial region, in contrast to Refs. [27–31]) and orbitals centered at atomic sites and confined to small nonoverlapping spheres. We refer to the latter as island orbitals (IOs) to distinguish them from the localized orbitals (LOs) of the extended LAPW methods [25,26]. The basis functions are derived from an approximation to the all-electron wave functions, which also has the PW + IO structure, and whose accuracy is regulated by the angular-momentum cutoff of the orbital part and by the $|\mathbf{k}+\mathbf{G}|$ cutoff of the plane-wave part. Owing to the orthogonality of the plane waves and to the finite domain of the orbitals, the basis set provides an efficient scheme for the matrix elements $\langle\mathbf{k}+\mathbf{q}\lambda'|\exp[i(\mathbf{q}+\mathbf{G})\cdot\mathbf{r}]|\mathbf{k}\lambda\rangle$. Thus, the Fourier representation $\epsilon_{\mathbf{GG}'}(\mathbf{q},\omega)$ is readily obtained, which is convenient, in particular because the Coulomb interaction becomes diagonal and because the reciprocal-lattice vector $\mathbf{G}$ is a natural cutoff parameter to systematically refine the accuracy of the DF.

To demonstrate the viability of the method we address the $\mathbf{q}$-dependent longitudinal DF of simple metals, focusing on the anisotropy of the plasmon dispersion. We analyze the similarities and differences in the anisotropy scenarios in Al and Na and explain the experimentally long-known opposite behavior of the anisotropy of the Drude plasmon relative to the low-energy zone-boundary collective state (ZBCS) [32] in

2469-9950/2019/99(24)/245149(11)

the two metals. Furthermore, we compare Al and Na with the less free-electron-like alkali metals Li, K, Rb, and Cs.

The paper is organized as follows: In the next section we describe the PW + IO representation of the wave functions and the resulting formalism for the DF. The accuracy and convergence of the product basis are analyzed in Appendix A. Computational aspects not related to the new method are presented in Sec. III. In Sec. IV, plasmon dispersion in aluminum and alkali metals is discussed. Appendix B presents an analysis of the effect of the semi-core polarization on the plasmon energy.

II. FORMALISM

Of all the band-structure methods, the formalism of augmented plane waves introduced by Slater [22] has the least limitations regarding the accuracy of the wave functions. Here, we consider an implementation for a basis of energy-independent APWs [23,24] extended by localized orbitals [25,26].

A. Filtering the all-electron wave function

The wave function $\psi_\lambda^{\mathbf{k}}$ for the Bloch vector $\mathbf{k}$ and band number λ is a sum of N_ξ APWs $\xi(\mathbf{r})$ and N_ζ localized orbitals $\zeta(\mathbf{r})$. For one atom per unit cell located at $\mathbf{r}=0$ it reads

$$\psi_\lambda^{\mathbf{k}}(\mathbf{r}) = \sum_{\mathbf{G}}^{N_\xi} p_{\mathbf{G}}^{\lambda\mathbf{k}} \xi_{\mathbf{G}}^{\mathbf{k}}(\mathbf{r}) + \sum_{lm}\sum_{\nu}^{\bar{\nu}_l} q_{\nu lm}^{\lambda\mathbf{k}} \zeta_{l\nu}(r) Y_{lm}(\hat{\mathbf{r}}). \qquad (1)$$

Here p and q comprise the set of variational coefficients, p being coefficients of the APWs and q of the LOs, and $\mathbf{G}$ are reciprocal-lattice vectors. The APW $\xi_{\mathbf{G}}^{\mathbf{k}}$ is smoothly continuous everywhere in the unit cell, and outside the muffin-tin (MT) spheres it coincides with the plane wave $\exp[i(\mathbf{k}+\mathbf{G})\cdot\mathbf{r}]$. The LOs vanish with their radial derivatives at the muffin-tin sphere and remain zero in the interstitial region. Subscript ν indicates the radial part of the local orbital, so $N_\zeta = \sum_l \bar{\nu}_l(2l+1)$.

In the sphere the angular-momentum expansion of the APW of a wave vector $\mathbf{K}=\mathbf{k}+\mathbf{G}$ reads

$$\xi_{\mathbf{G}}^{\mathbf{k}}(\mathbf{r}) = \sum_{lm} [A_{lm}(\mathbf{K})\phi_l(r) + B_{lm}(\mathbf{K})\dot{\phi}_l(r)] Y_{lm}(\hat{\mathbf{r}}), \qquad (2)$$

where ϕ_l is a solution of the radial Schrödinger equation and $\dot{\phi}_l$ is its energy derivative [23,24]. Coefficients A_{lm} and B_{lm} are determined from the condition that the APW be smoothly continuous at the sphere boundary, $r=S$. Thus, for each l the radial basis comprises $\bar{n}_l = \bar{\nu}_l + 2$ functions u_{ln}, where $u_{l1}=\phi_l$, $u_{l2}=\dot{\phi}_l$, and the radial part of the LO is a linear combination of three functions: $\zeta_{l\nu} = u_{l(\nu+2)} + a_{l\nu}\phi_l + b_{l\nu}\dot{\phi}_l$. Usually, $u_{l(\nu+2)}$ are also radial solutions for different energies, although in some applications they may be more complicated functions [33,34].

A straightforwardly constructed set of products of $N = N_\xi + N_\zeta$ functions would comprise $N(N+1)/2$ terms, of which a much smaller number are linearly independent and physically relevant. There is no universal recipe to *a priori* select the optimal subset—without reference to the specific shape of the APWs—although some intuitive criteria and practical schemes were suggested in Refs. [20,27]. Here we develop an approach that avoids an explicit construction of the products of the APWs, but instead employs an approximate (filtered) representation of the wave functions to generate the product basis. This approximate representation has the property that both the accuracy of the filtered wave functions and the completeness of the product basis are naturally controlled by a *spatial resolution criterion*, i.e., by the $\mathbf{G}$-vector cutoff of the PW set and by the lm cutoff of the IO set.

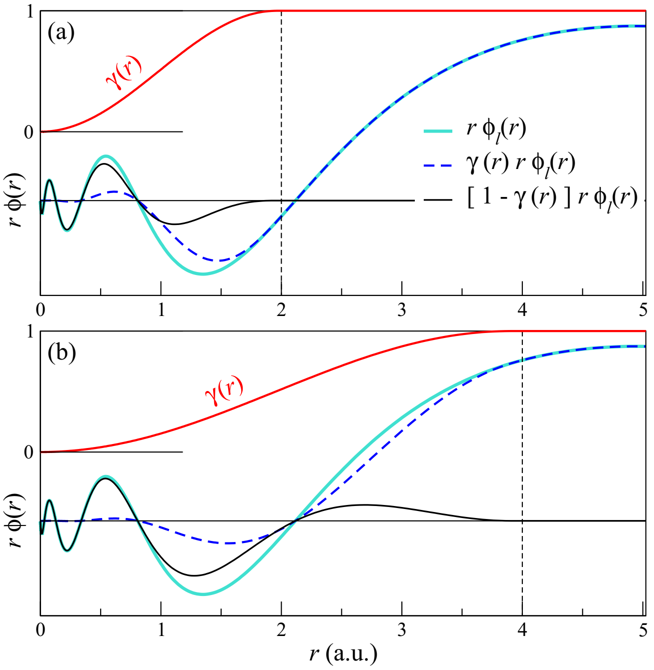

FIG. 1. γ partitioning in the sphere of Cs for (a) $S_\gamma = 2$ a.u. and (b) $S_\gamma = 4$ a.u: radial solution (thick light-blue line) is multiplied by $\gamma(r)$ (thick red line). The gouging radii S_γ are indicated by vertical dashed lines, and the MT radius is 5.02 a.u. The radial function is for $l=0$, and energy is at the Fermi level.

To arrive at the optimal partitioning between the PW and IO components of the filtered wave function, we first modify the original wave function ψ by damping its rapid oscillations in the vicinity of the nuclei: within a sphere of radius S_γ (smaller than the muffin-tin radius, see Fig. 1) we multiply ψ by a function $\gamma(r)$ that is zero at $r=0$ and steadily grows to reach unity at $r=S_\gamma$:

$$\gamma(r) = \begin{cases} \frac{1}{2}\left(1-\cos\frac{\pi r}{S_\gamma}\right) & \text{for } r \leqslant S_\gamma \\ 1 & \text{for } r > S_\gamma. \end{cases} \qquad (3)$$

The gouged function $\gamma\psi$ has a rapidly convergent plane-wave expansion [35,36], which constitutes the Fourier part ψ^{F} of the filtered wave function:

$$\psi = \gamma\psi + (1-\gamma)\psi \approx \psi^{\mathrm{F}} + (1-\gamma)\psi \approx \psi^{\mathrm{F}} + \psi^{\mathrm{I}}. \qquad (4)$$

Here ψ^{I} is an approximation to $(1-\gamma)\psi$ obtained by truncating the angular-momentum expansion of ψ. It consists of isolated islands around the nuclei, and the smaller the radius S_γ of the island the faster converges the lm series of ψ^{I} and the slower does the PW series of ψ^{F}. For sufficiently small γ spheres, ψ^{I} can be completely neglected to a good approximation [35,36]. In Appendix A, we present a detailed study of the convergence and accuracy of the $\psi^{\mathrm{F}} + \psi^{\mathrm{I}}$ representation.

B. Density matrix elements

Let us consider the operator $\hat{o} = \exp(i\mathbf{Q}\cdot\mathbf{r})$, where $\mathbf{Q} = \mathbf{q} + \mathbf{G}$. Using the notation $\psi_\lambda = \langle \mathbf{r}|\psi_\lambda\rangle$, $\psi^{\mathrm{F}}_\lambda = \langle \mathbf{r}|F_\lambda\rangle$, and $\psi^{\mathrm{I}}_\lambda = \langle \mathbf{r}|I_\lambda\rangle$ for the approximate wave functions $\psi_\lambda = \psi^{\mathrm{F}}_\lambda + \psi^{\mathrm{I}}_\lambda$ given by Eq. (4) we write the matrix element $\langle\psi_\lambda|\hat{o}|\psi_\mu\rangle$ as a sum of an integral over the entire unit cell $\langle F_\lambda|\hat{o}|F_\mu\rangle$ and three integrals over the small γ spheres:

$$\langle\psi_\lambda|\hat{o}|\psi_\mu\rangle = \langle F_\lambda|\hat{o}|F_\mu\rangle + \langle F_\lambda|\hat{o}|I_\mu\rangle + \langle I_\lambda|\hat{o}|F_\mu\rangle + \langle I_\lambda|\hat{o}|I_\mu\rangle. \tag{5}$$

The first term on the right-hand side is readily calculated via plane waves, and the integrals over the γ spheres can be calculated in the angular-momentum representation in view of the relation $\psi^{\mathrm{F}} \approx \gamma\psi$; see Eq. (4). Their sum reduces to $\langle\psi_\lambda|\hat{o}|\psi_\mu\rangle_\gamma - \langle F_\lambda|\hat{o}|F_\mu\rangle_\gamma$, where the subscript γ indicates that the integration is limited to the γ spheres. The computational efficiency of this scheme stems from the following properties: First, the lm series converges fast because the γ spheres are small, and it is helpful that the coefficients are the same for the wave function ψ and for its Fourier-filtered part ψ^{F}. Second, the plane-wave expansion of $\gamma\psi$ contains a reasonable number of plane waves because—in contrast to the energy-eigenvalue problem—a high accuracy close to the nucleus is not needed (see Appendix A). Note that the approximate function (4) is smoothly continuous by construction at any l cutoff, whereas in the original APW representation one has to include rather high angular momenta to achieve the continuity. This property is important, in particular for the construction of the effective potentials from orbital-dependent functionals [37].

The operator $\exp[i(\mathbf{q}+\mathbf{G})\cdot\mathbf{r}]$ is diagonal in the PW basis, so the first term in Eq. (5) is easy to calculate. Let $F^{\mathbf{k}\lambda}_{\mathbf{G}}$ be the coefficients of the plane waves $\exp[i(\mathbf{k}+\mathbf{G})\mathbf{r}]$ in the expansion of the PW part of the filtered wave function in Eq. (4). Then the first term on the right-hand side of Eq. (5) is

$$\left\langle F^{\mathbf{k+q}}_{\lambda'}\middle| e^{i(\mathbf{q}+\mathbf{G})\cdot\mathbf{r}}\middle|F^{\mathbf{k}}_{\lambda}\right\rangle = V\sum_{\mathbf{G}'}\left[F^{\mathbf{k+q}\lambda'}_{\mathbf{G}'+\mathbf{G}}\right]^* F^{\mathbf{k}\lambda}_{\mathbf{G}'}. \tag{6}$$

The contribution from the islands is obtained from the angular-momentum decomposition of the wave functions inside the muffin-tin spheres:

$$\psi^{\mathbf{k}}_\lambda(\mathbf{r}) = \sum_l^{l_{\max}}\sum_n^{\bar{n}_l}\sum_{m=-l}^{l} C^{\mathbf{k}\lambda}_{lnm}u_{ln}(r)Y_{lm}(\hat{\mathbf{r}}) \tag{7}$$

using the Rayleigh expansion of $\exp(i\mathbf{Q}\cdot\mathbf{r})$:

$$\begin{aligned}&\left\langle\psi^{\mathbf{k+q}}_{\lambda'}\middle|e^{i\mathbf{Q}\cdot\mathbf{r}}\middle|\psi^{\mathbf{k}}_{\lambda}\right\rangle_\gamma - \left\langle F^{\mathbf{k+q}}_{\lambda'}\middle|e^{i\mathbf{Q}\cdot\mathbf{r}}\middle|F^{\mathbf{k}}_{\lambda}\right\rangle_\gamma\\ &= \sum_{ll'}^{l_{\max}}\sum_{nn'}\sum_{mm'}\left[C^{\mathbf{k+q}\lambda'}_{l'n'm'}\right]^* C^{\mathbf{k}\lambda}_{lnm}\\ &\quad\times\sum_{l''}^{l''_{\max}} T^{l''}_{ll'mm'}(\hat{\mathbf{Q}})\int_0^{S_\gamma} j_{l''}(Qr)U_{ll'nn'}(r)dr,\end{aligned} \tag{8}$$

where the angular integration yields

$$T^{l''}_{ll'mm'}(\hat{\mathbf{Q}}) = 4\pi i^{l''}Y^*_{l''m''}(\hat{\mathbf{Q}})\int Y^*_{l'm'}Y_{l''m''}Y_{lm}\,d\hat{\mathbf{r}}. \tag{9}$$

Here lm and $l'm'$ refer to the angular-momentum decomposition of $\psi^{\mathbf{k}}_\lambda$ and $\psi^{\mathbf{k+q}}_{\lambda'}$, respectively, and l'' refers to the Rayleigh expansion of $\exp(i\mathbf{Q}\cdot\mathbf{r})$. The radial functions

$$U_{ll'nn'}(r) = u_{l'n'}(r)u_{ln}(r)[1-\gamma(r)^2]r^2 \tag{10}$$

are products of the radial parts of APWs multiplied by the confining function $[1-\gamma(r)^2]r^2$. Because the radii S_γ are independent of the other computational parameters they can be chosen rather small, typically 1 to 2 a.u., so that the angular-momentum sums can be truncated at rather low l, as will be demonstrated in the next section. To summarize, the PW + IO product basis set consists of plane waves $\exp[i(\mathbf{q}+\mathbf{G})\cdot\mathbf{r}]$ and island orbitals $U_{ln}(r)Y_{lm}(\hat{\mathbf{r}})$ whose radial shape is given by Eq. (10) and angular part by Eq. (9). The matrix element of $\exp[i(\mathbf{q}+\mathbf{G})\cdot\mathbf{r}]$ is a sum of expressions (6) and (8).

The size of the set scales linearly with the size of the unit cell, and the IO part can be further reduced by removing the linearly dependent IOs [20,21,27,28,38]. According to Eq. (10), for each pair of l and l' the set of radial products comprises $\bar{n}_l \times \bar{n}_{l'}$ functions, and large $\bar{n}_l$ may be needed to describe a wide energy interval. For example, in order to achieve convergence of the *GW* method with respect to the number of unoccupied states it may be necessary to include up to $\bar{n}_l = 8$ radial functions per lm channel [29,31,39]. A straightforward inclusion of all the products $u_{l'n'}u_{ln}$ may lead to an excessively large and linearly dependent basis set. Here, we can take advantage of the fact that $U_{ll'nn'}(r)$ are restricted to a close vicinity of the potential singularity, where the radial solutions change very slowly with energy [23,34], so the number of physically relevant u_{ln} is much smaller. Moreover, their shape is determined by the potential singularity, and it is practically independent of the crystal potential. Thus, for a given S_γ, the functions $U_{ll'nn'}(r)$ can be tabulated for each element.

To demonstrate how a relevant set can be selected out of a full set of functions $U_{ll'nn'}(r)$, let us take the MT sphere of Cu as an example and consider the contribution of the d orbitals to the spherical part $l'' = 0$ of Eq. (8). The $3d$ band is described by the radial solution at the energy $E = -3$ eV relative to the Fermi level and by its energy derivative. The radial set is extended by a $4d$ and a $5d$ function at $E = 40$ and 133 eV, respectively. This gives rise to $N_U = 10$ functions $U_{llnn'}(r)$ with $l = 2$. We now diagonalize the overlap matrix of the functions $U_{llnn'}(r)$ and retain only the eigenvectors of eigenvalues larger than some predefined ε. The number N_ε of the retained functions is smaller for smaller gouging radius S_γ. We then fit the N_U original functions with the N_ε orthogonal functions and in Fig. 2(a) present the maximal error $\|\delta(N_\varepsilon, S_\gamma)\|$ as a function of S_γ. Figure 2(b) shows the performance of the orthogonal set in the sphere of Cs for four p orbitals comprising ϕ and $\dot{\phi}$ at the $5p$ branch and two ϕ functions at the $6p$ and $7p$ branches. Thus, the accuracy with which the radial part of the product set is represented is flexibly adjusted by the gouging radius and by the number of the orthogonal basis functions.

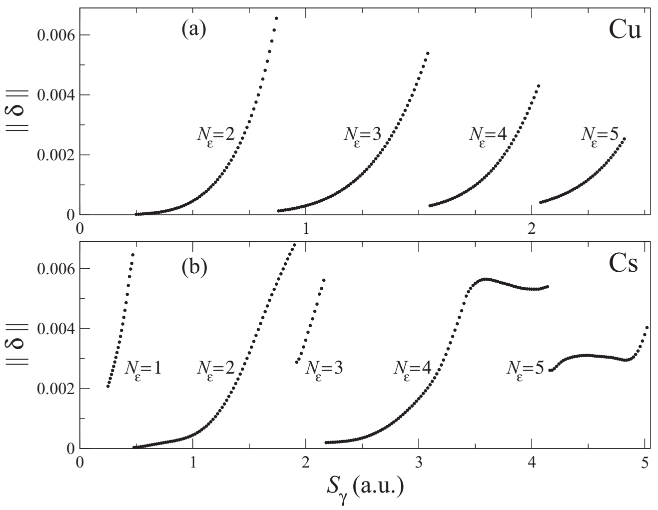

FIG. 2. Accuracy of the representation of the radial density matrix $U_{ll'nn'}(r)$ by a reduced orthogonal basis set; see last paragraph of Sec. II B. The error $\|\delta(N_\varepsilon, S_\gamma)\|$ is shown for the products of (a) the *d* orbitals of Cu and (b) the *p* orbitals of Cs. The overlap eigenvalue cutoff is $\varepsilon = 0.0001$.

The data on the accuracy of the product-set expansion regarding the number of PWs in ψ^{F} and IOs in ψ^{I}, Eq. (4), as well as on the l'' convergence of the $\exp(i\mathbf{q}\cdot\mathbf{r})$ operator, Eq. (8), are given in Appendix A. To verify the applicability of Eq. (8) to larger wave vectors, which appear in the nondiagonal elements of the microscopic DF, we show in Fig. 8 the data for q up to 4 Å^{-1}. For sufficiently large S_γ the number of PWs may be chosen comparable to the number of APWs, while a reduction of S_γ significantly accelerates the angular-momentum convergence.

III. CALCULATION OF PLASMON ENERGY

In this work we are mainly interested in the plasmon dispersion in Al and Na, where the plasmon energy is well above the intense interband transitions and, at the same time, it is well below the onset of semi-core excitations, 65 eV in Al and 25 eV in Na. In such cases the local fields can be neglected to a good approximation [40–42], and DF reduces to the following expression within the random-phase approximation (RPA) [43]:

$$\epsilon(\mathbf{q},\omega) = 1 - \frac{8\pi}{q^2 V}\sum_{\lambda\lambda'\mathbf{k}} \frac{|\langle\lambda'\mathbf{k}+\mathbf{q}|\exp{(i\mathbf{q}\cdot\mathbf{r})}|\lambda\mathbf{k}\rangle|^2}{E_{\lambda'\mathbf{k}+\mathbf{q}} - E_{\lambda\mathbf{k}} - \hbar\omega + i\eta}, \quad (11)$$

where the summation is over occupied states $|\lambda\mathbf{k}\rangle$ and unoccupied states $|\lambda'\mathbf{k}+\mathbf{q}\rangle$. The imaginary part $\epsilon_2(\mathbf{q},\omega)$ is calculated in the limit $\eta \to 0$ with the linear tetrahedron interpolation in $\mathbf{k}$ space [44], and the real part is obtained via the Kramers–Kronig relation. (The ϵ_2 spectrum cutoff was chosen so as to include the transitions from the semi-core states.) The convergence of the plasmon energies with respect to the $\mathbf{k}$-point sampling is rather slow: For example, for Al, $\psi_\lambda^{\mathbf{k}}$ are calculated on a $71\times71\times71$ mesh in the reciprocal-lattice cell, of which the irreducible $\mathbf{k}$ points are selected depending on the symmetry of the vector $\mathbf{q}$. For $\mathbf{q}\parallel[100]$ this yields 47 286 irreducible $\mathbf{k}$ points and 273 492 irreducible tetrahedra. The complex DF of Al for $\mathbf{q}\parallel[100]$ and $\mathbf{q}\parallel[110]$ is shown in Fig. 3 for $q = 0.5$ and 0.75 Å^{-1}. The spectra agree well with the pseudopotential calculations by Lee and Chang [49]. Figure 3 also shows a high-energy part of the loss function $L(\mathbf{q},\omega) = -\mathrm{Im}[1/\epsilon(\mathbf{q},\omega)]$, whose maximum above the intense interband transitions is referred to as the Drude plasmon because it can be related to the jellium model [50]. The $\epsilon_2(\omega)$ spectrum is seen to be strongly anisotropic: a zone-boundary gap (ZB) is very pronounced for $\mathbf{q}\parallel[100]$ and is much weaker for $\mathbf{q}\parallel[110]$. For $\mathbf{q}\parallel[100]$ this structure gives rise to a very sharp low-energy peak in the loss function, see Fig. 4(c). This is the well-known zone-boundary collective state first predicted for simple metals by Foo and Hopfield [32].

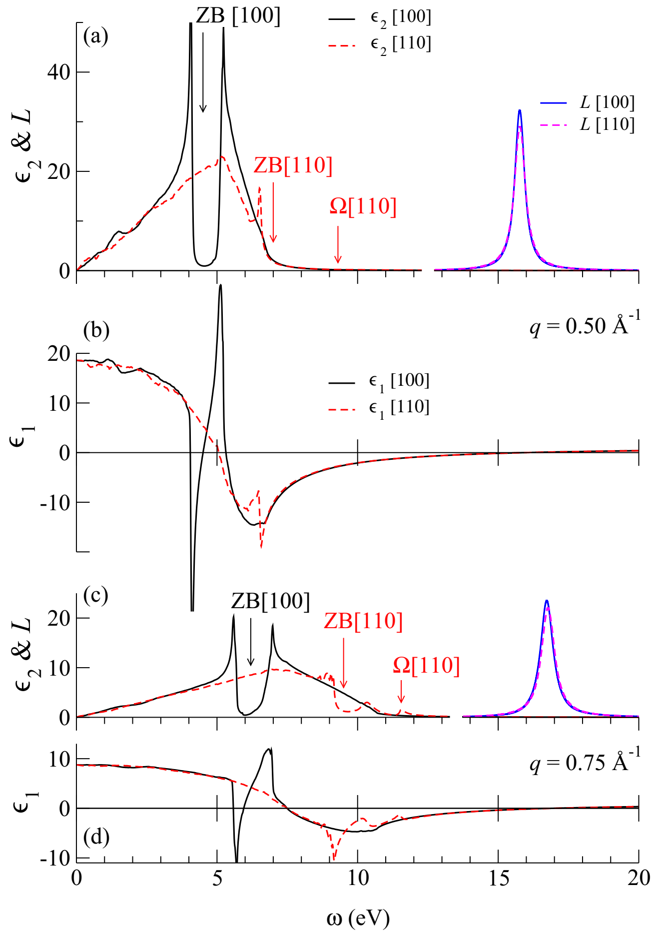

FIG. 3. Real ϵ_1 and imaginary ϵ_2 parts of the DF and loss function $L = -\mathrm{Im}(1/\epsilon)$ of Al for (a), (b) $q = 0.5$ Å^{-1}, and (c), (d) 0.75 Å^{-1},. Full lines are for $\mathbf{q}\parallel[100]$ and dashed lines for $\mathbf{q}\parallel[110]$. Vertical arrows marked ZB[110] indicate a zone-boundary gap, and Ω[110] indicates a maximum at the high-energy slope of the spectrum; see Sec. IV and Fig. 5.

The dispersion $\omega_{\mathrm{p}}(q)$ of the Drude plasmon is shown in Fig. 4(a) for $\mathbf{q}\parallel[100]$ and $\mathbf{q}\parallel[110]$. Let us extrapolate the dispersion curves to $q = 0$ by fitting the calculated $\omega_{\mathrm{p}}(q)$ points with a Lindhard-like function $\omega_{\mathrm{p}}(q) = \omega_{\mathrm{p}}(0) + \alpha q^2 + \beta q^4$; see Table I. For Al we obtain $\omega_{\mathrm{p}}(0) = 15.02$ eV, which is in accord with the measured value $\omega_{\mathrm{p}}(0) = 15.01 \pm 0.01$ eV [46] but strongly deviates from the value of 15.28 eV

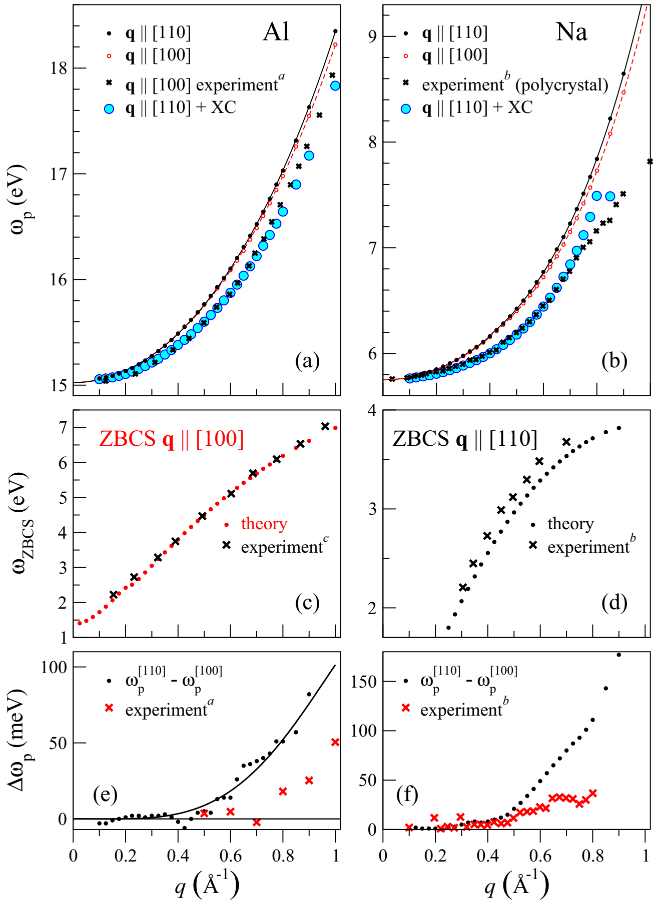

FIG. 4. Plasmon dispersion in Al (left column) and Na (right column). (a), (b) Dispersion of the Drude plasmon for $\mathbf{q} \parallel [110]$ (full black circles) and $\mathbf{q} \parallel [100]$ (open red circles) within the RPA and with the XC correction [45] (large blue circles). (c), (d) Dispersion of ZBCS for $\mathbf{q} \parallel [100]$ for Al and for $\mathbf{q} \parallel [110]$ for Na. (e), (f) Anisotropy of the Drude plasmon. Crosses show the measurements of Refs. [46]^a, [47]^b, and [48]^c (extracted from graphical data).

calculated in Ref. [49]. The main reason for this is the neglect of the core polarization in the pseudopotential calculation of Ref. [49]; see Appendix B. For Na the agreement is equally good: $\omega_\mathrm{p}(0) = 5.75$ eV in our theory and 5.76 ± 0.02 eV in experiment [47] (extracted from graphical data).

Apart from fundamental approximations, the theoretical results suffer from the computational uncertainty of $\epsilon(\omega)$. Indeed, the plasmon energy is determined by the condition $\epsilon_1(\omega_\mathrm{p}) = 0$, and for a small slope $d\epsilon_1(\omega)/d\omega$ it becomes very sensitive to small errors in $\epsilon_1(\omega)$. The most important source of error is the inaccuracy of the wave functions $\langle \mathbf{r}|\lambda\mathbf{k}\rangle$, which results in an error in the numerator of Eq. (11). This is an inevitable shortcoming of the variational wave functions, which stems from the incompleteness of the basis set. Its effect on the accuracy of ω_p can be estimated by comparing a numerical $q \to 0$ limit by Eq. (11) with the calculation in the optical limit $q = 0$. In the latter case the intraband part $\lambda = \lambda'$ acquires the Drude form $\epsilon_1(\omega) = 1 - \omega_0^2/\omega^2$. For a cubic crystal, ω_0^2 is the diagonal element of the plasma frequency tensor $\omega_0 = \omega_{xx} = \omega_{yy} = \omega_{zz}$ given by the integral over the Fermi surface

$$\omega^2_{\mu\nu} = \frac{1}{\pi^2}\sum_{\lambda}\int \frac{v_\mu(\lambda\mathbf{k})v_\nu(\lambda\mathbf{k})}{|\mathbf{v}(\lambda\mathbf{k})|}dS_\mathrm{F}, \qquad (12)$$

where μ and ν indicate Cartesian components of the group velocity $\mathbf{v}(\lambda\mathbf{k})$ in the state $|\lambda\mathbf{k}\rangle$. For $\lambda \neq \lambda'$ the numerator of Eq. (11) reduces to the squared modulus of the momentum matrix element $\langle\lambda'\mathbf{k}|\hat{\mathbf{p}}|\lambda\mathbf{k}\rangle$:

$$\lim_{q\to 0}\langle\lambda'\mathbf{k}+\mathbf{q}|\exp{(i\mathbf{q}\cdot\mathbf{r})}|\lambda\mathbf{k}\rangle = \frac{\hbar}{m}\frac{\langle\lambda'\mathbf{k}|\mathbf{q}\cdot\hat{\mathbf{p}}|\lambda\mathbf{k}\rangle}{E_{\lambda'\mathbf{k}} - E_{\lambda\mathbf{k}}}. \qquad (13)$$

In the optical limit we obtain for Al $\omega_\mathrm{p}^\mathrm{opt} = 14.92$ eV and for Na $\omega_\mathrm{p}^\mathrm{opt} = 5.72$ eV, i.e., the uncertainty of ω_p amounts to 0.10 eV in Al and 0.03 eV in Na. According to our analysis, most of the error comes from the numerator of the interband term in Eq. (11), and there are two reasons whyit is larger in Al than in Na. First, the slope of the $\epsilon_1(\omega)$ curve at ω_p is much smaller in Al than in Na: $d\epsilon_1(\omega)/d\omega = 0.13\ \mathrm{eV}^{-1}$ in Al and $0.35\ \mathrm{eV}^{-1}$ in Na. Second, at $q \to 0$ interband transitions play much larger role in Al than in Na. In Al, the intrinsic uncertainty in $\epsilon_1(\omega_\mathrm{p})$ is 0.013, which is ~4% of the interband contribution. The error stems from the inaccuracy of the $\psi_\lambda^\mathbf{k}$ themselves, and it far exceeds the error due to the approximate treatment of the products $\psi_{\lambda'}^{\mathbf{k}*}\psi_\lambda^{\mathbf{k}-\mathbf{q}}$ with a computationally reasonable product basis set, as we show in Appendix A.

TABLE I. Fitting the plasmon dispersion in Al with the function $\omega_\mathrm{p}(q) = \omega_\mathrm{p}(0) + \alpha q^2 + \beta q^4$. XC indicates that a static exchange-correlation correction is included.

	$\omega_\mathrm{p}(0)$ (eV)	α (eV Å^2)	β (eV Å^4)
This work $\mathbf{q} \parallel [100]$	15.02	2.81	0.38
This work $\mathbf{q} \parallel [110]$	15.02	2.80	0.50
This work $\mathbf{q} \parallel [100]$ (XC)	15.02	2.12	0.50
This work $\mathbf{q} \parallel [110]$ (XC)	15.02	2.10	0.69
Experiment [46]	15.01	2.27	0.65
Theory [49] (XC)	15.28	2.13	0.58

IV. ANISOTROPY OF PLASMON DISPERSION

The basic aspects of the DF of nearly free-electron metals can be understood from the Lindhard formula for jellium [50], but the band-structure effects have long been realized to be important [51]. In particular, zone-boundary collective states were identified in Al [52] and in Li and Na [53]. The relation between the underlying band structure and the energy-loss function was analyzed for Al [49,54,55] and for alkali metals [40,41,56–59], also under pressure [60–66]. In cesium, the interband transitions were found to cause a negative plasmon dispersion [40,41]. Many works addressed the role of the crystal local field and exchange and correlation (XC) in the dielectric response: the effect of the many-body interactions on the plasmon dispersion was studied for Al and for alkalis in Refs. [40–42,57–59,61,65,67–69]. It was concluded that the local field effects are almost negligible unless the semi-core states are involved [40–42].

Obviously, the anisotropic band structure should lead to the anisotropy of the loss function. The directional

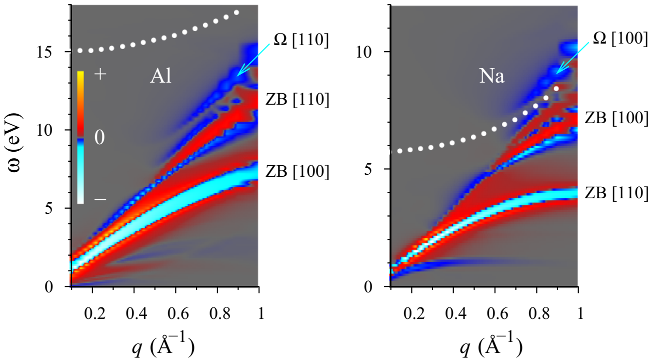

FIG. 5. Energy-momentum map of the anisotropy of ϵ_2: left graph shows $\omega\epsilon_2^{[100]} - \omega\epsilon_2^{[110]}$ for Al and right graph shows $\omega\epsilon_2^{[110]} - \omega\epsilon_2^{[100]}$ for Na. White circles show the location of the Drude plasmon.

dependence of the plasmon dispersion was studied experimentally in Al [46,70,71], Na [47], and Li [72] and theoretically analyzed by using model approaches [51,53,73] and from first principles [49,57,58,67,69]. In Al and Na the anisotropy of the Drude plasmon is rather subtle: experimentally, the difference $\Delta\omega_\mathrm{p} = \omega_\mathrm{p}^{[110]} - \omega_\mathrm{p}^{[100]}$ reaches ≈0.05 eV around 1 Å^{-1} [46,47]; see Figs. 4(e) and 4(f). The theoretical estimates based on a local pseudopotential model of Bross [51] and on the *ab initio* pseudopotential study by Lee and Chang [49] gave $\Delta\omega_\mathrm{p} = 0.2$ and 0.25–0.30 eV, respectively. On the contrary, in the *ab initio* pseudopotential calculation by Quong and Eguiluz [57] no anisotropy was resolved.

It is tempting to relate the anisotropy of $\omega_\mathrm{p}(q)$ to the most conspicuous anisotropic feature of the $\epsilon_2(\mathbf{q}, \omega)$ spectrum, the zone-boundary gap; see Fig. 3. However, obviously, this feature cannot explain the observation. First, both experimentally and theoretically, Al and Na behave oppositely with respect to the ZBCS: in Al, ZBCS occurs for $\mathbf{q}\,\|\,[100]$ and in Na for $\mathbf{q}\,\|\,[110]$, whereas both in Al and in Na it is $\omega_\mathrm{p}^{[110]} > \omega_\mathrm{p}^{[100]}$. Second, $\Delta\omega_\mathrm{p}$ grows with increasing q, whereas the influence of the ZB gap decreases, as illustrated by the difference $\epsilon_2^{[100]} - \epsilon_2^{[110]}$ for Al (and opposite function for Na) shown in Fig. 5. The energy-momentum distributions of the anisotropy are seen to be very similar in Al and Na, with Na[110] playing the role of Al[100] and Na[100] the role of Al[110]. In Al, the ϵ_2 spectrum for $\mathbf{q}\,\|\,[110]$ has a more complicated structure than for $\mathbf{q}\,\|\,[100]$: apart from the low-energy gap (denoted ZB[110] in Figs. 3 and 5), at larger q there emerges a maximum (denoted Ω[110]) at the high-energy slope of the spectrum. Its contribution to $\epsilon_1(\omega_\mathrm{p})$ grows with q, and because it appears below $\omega_\mathrm{p}^{[110]}$ it shifts $\omega_\mathrm{p}^{[110]}$ to higher energies. A similar picture takes place for Na, only there is an additional dip-peak structure between ZB[100] and Ω[100], see Fig. 5. However, the effect is the opposite: in Na the Ω[100] peak occurs *above* the plasmon energy, so that it shifts $\omega_\mathrm{p}^{[100]}$ to lower energies.

Thus, the opposite behavior of the anisotropy of the Drude plasmon relative to ZBCS in Al and Na is explained by the different location of the uppermost structure Ω relative to ω_p. Furthermore, Fig. 5 explains why both in Al and in Na the anisotropy is negligible below and rapidly grows above $q =$ 0.5 Å^{-1}; see Figs. 4(e) and 4(f). It is at this wave vector that the Ω structure appears in the spectrum. Within the RPA, the difference between the measured and the calculated energies of the Drude plasmon is of the same order of magnitude in Al and Na. The discrepancy is largely due to the neglect of exchange and correlation. These effects can be approximately included by a static local field correction function $G(q)$ using the parametrization of Utsumi and Ichimaru [45]:

$$\epsilon(\mathbf{q}, \omega) \to 1 + \frac{\epsilon(\mathbf{q}, \omega) - 1}{1 - G(q)[\epsilon(\mathbf{q}, \omega) - 1]}. \tag{14}$$

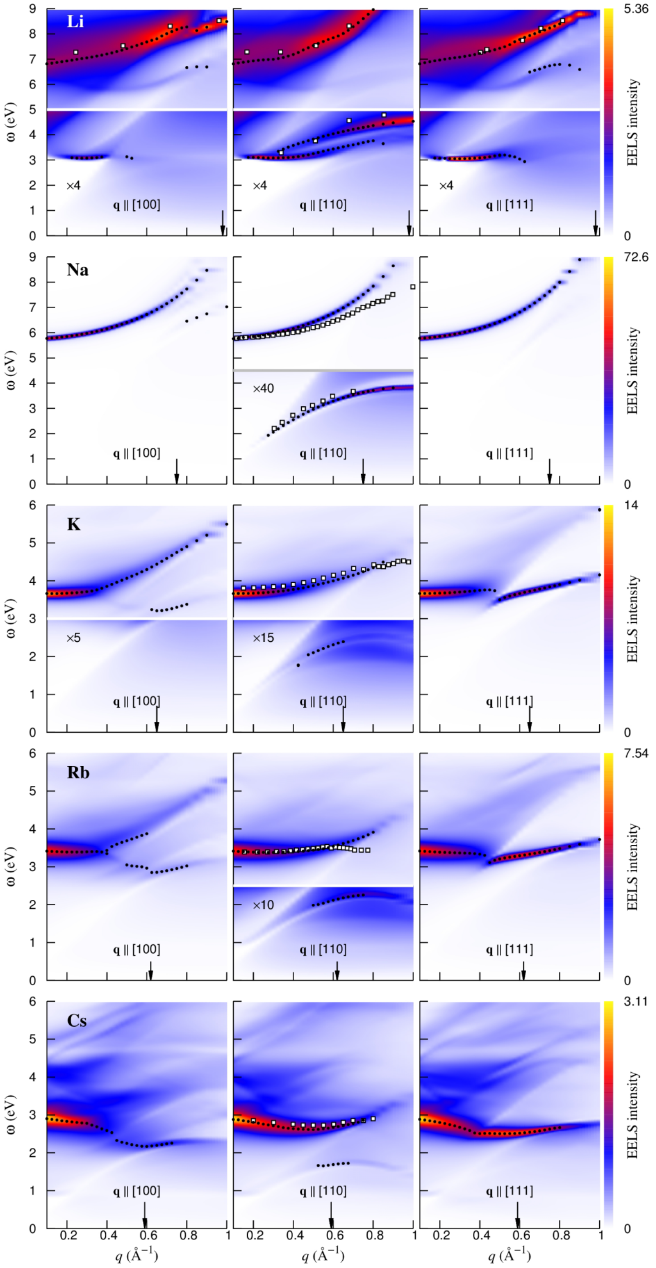

FIG. 6. Calculated energy-loss spectra of Li, Na, K, Rb, and Cs for $\mathbf{q}\,\|\,[100]$, $\mathbf{q}\,\|\,[110]$, and $\mathbf{q}\,\|\,[111]$. White squares are experimental data of Refs. [72,74] for Li and of Ref. [47] for Na, K, Rb, and Cs. Black circles show the plasmon location, i.e., $\epsilon_1(q, \omega) = 0$. The vertical arrows indicate the critical q values of the Lindhard model. Note the scale change indicated by the horizontal white line.

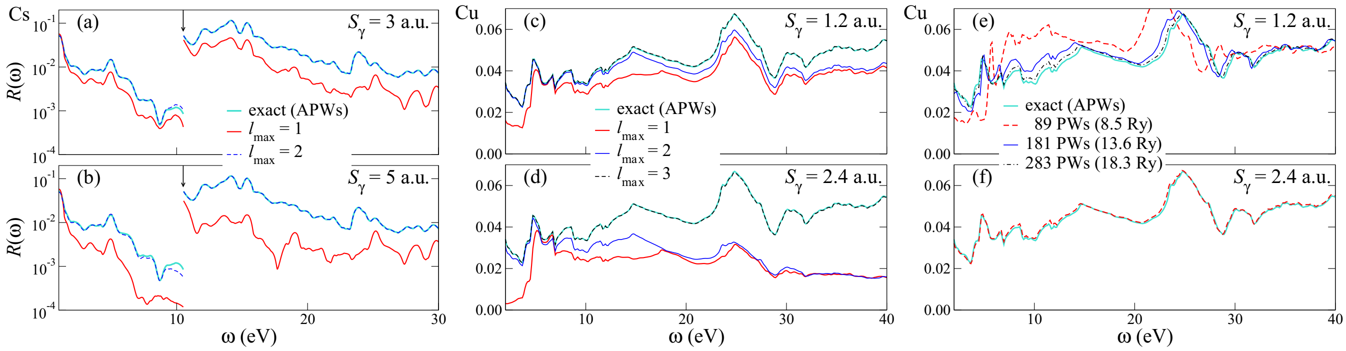

FIG. 7. (a)–(d) Convergence of MME with the angular-momentum cutoff l_{max}. (e), (f) Convergence of MME with the number of plane waves. (a), (b) For Cs, **k**-averaged MME $R(\omega)$ are shown in logarithmic scale for (a) $S_\gamma = 3$ a.u. and (b) $S_\gamma = 5$ a.u. The Fourier part comprises 229 PWs. Vertical arrows in the upper ω axes mark the onset of the semi-core transitions. For Cu, $S_\gamma = 1.2$ a.u. in panels (c) and (e) and $S_\gamma = 2.4$ a.u. in panels (d) and (f). In panels (c) and (d), the Fourier part comprises 459 PWs. In panels (e) and (f), the convergence with the number of PWs is for $l_{\text{max}} = 4$. The cutoff energy $|\mathbf{G}|^2$ is given in parentheses.

The XC correction brings the plasmon dispersion in Na into excellent agreement with the experiment over the interval up to $q = 0.75$ Å^{-1}; see Fig. 4(b). For Al, the XC correction transforms the $\omega_{\text{p}}(q)$ curve in a similar way, see Fig. 4(a), but the parameter α is strongly underestimated, see Table I.

In contrast to Al and Na, in alkali metals Li, K, Rb, and Cs the interband transitions around the plasmon energy are rather intense; see Fig. 6. Their strong energy dependence causes more-or-less pronounced irregularities in the plasmon dispersion accompanied by a strong damping (large spectral width) of the plasmon. Also the anisotropy of $\epsilon_2(\omega)$ is very strong, which leads to a rather different shape of the plasmon dispersion curve for different directions of **q**; see Fig. 6.

Figure 6 show the loss function of alkali metals for $\mathbf{q} \parallel [100]$, $\mathbf{q} \parallel [110]$, and $\mathbf{q} \parallel [111]$ in comparison with the experiment. In Li, we again observe both the Drude plasmon at $\omega_{\text{p}}(0) = 6.72$ eV and the ZBCS. For $\mathbf{q} \parallel [110]$, in our calculation two ZBCS branches are resolved. In K, the plasmon peaks are much sharper than in Li, but the band-structure effects are, evidently, very strong: the plasmon dispersion is far from parabolic, and its shape is considerably different for different directions. For $\mathbf{q} \parallel [110]$, the agreement with the experiment [47] is rather good. (In contrast with Al and Na, in K the experimental curve lies slightly above the theoretical one.) In Rb and Cs, the unoccupied 3d states come closer to the Fermi level, and the strong dipole transitions to these states are responsible for the pronouncedly non-free-electron behavior of the DF [40]: in Rb the plasmon disperses only weakly, and in Cs the function $\omega_{\text{p}}(q)$ is nonmonotonic, with a minimum at ~0.5 Å^{-1} in agreement with the experiment [47]. Our result is in good agreement with the pseudopotential calculation of Ref. [41].

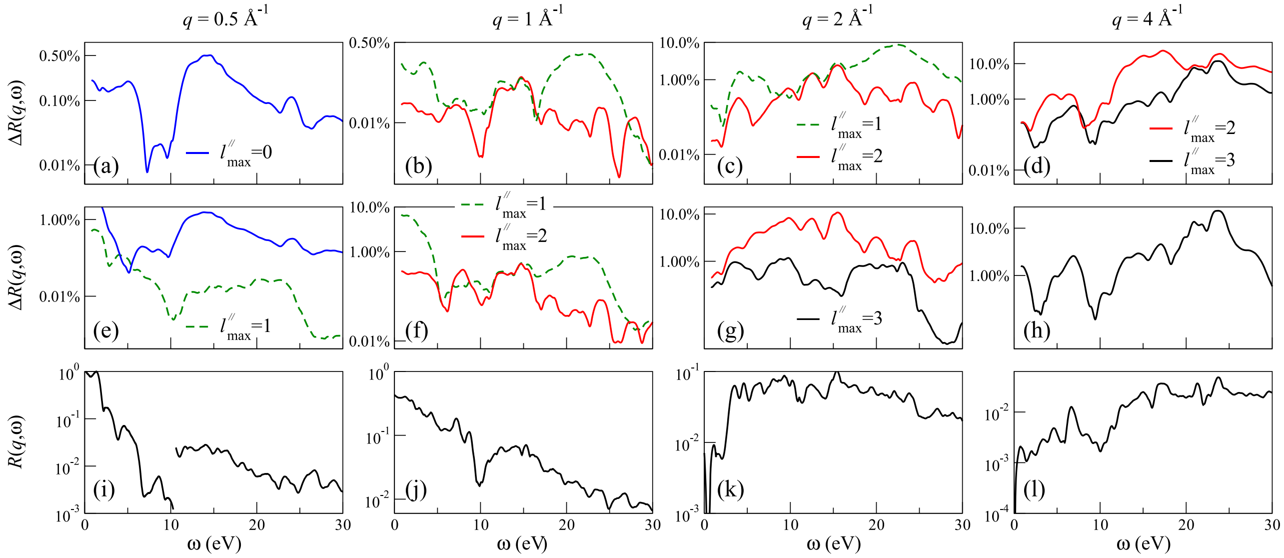

FIG. 8. Convergence of the Rayleigh expansion of $\exp(i\mathbf{q}\cdot\mathbf{r})$ for Cs for $\mathbf{q} \parallel [100]$ for $q = 0.5$, 1.0, 2.0, and 4.0 Å^{-1} for (a)–(d) $S_\gamma = 3$ a.u. and (e)–(h) $S_\gamma = 5$ a.u. The lowest row shows the reference spectrum $\bar{R}(q,\omega)$ calculated with $l''_{\text{max}} = 4$; see Eq. (8). The upper rows show **k**-averaged values of the error $\Delta R(l''_{\text{max}}) = |R(l''_{\text{max}}) - \bar{R}|$ with $l_{\text{max}} = 0$ to 3 [in percent relative to the average value of $\bar{R}(q,\omega)$ over the spectrum; note the logarithmic scale]. The Fourier part comprises 959 PWs.

V. SUMMARY

We have developed a product basis set to represent response functions within an all-electron framework. The proposed basis set consists of plane waves defined over the whole space and spatially restricted orbitals, with the spatial dependence of the response function being smoothly continuous by construction. It has a number of physically appealing and computationally convenient properties. In particular, it can be defined universally, without regard to the computational parameters of the band-structure method (such as muffin-tin radii, energy parameters, and number of APWs in LAPW). Consequently, the accuracy with which the physically relevant response is represented can be set *a priori* and balanced with the intrinsic accuracy of the underlying band-structure calculation. Depending on the specific application, the basis set can be optimized by tuning the relative weight carried by PWs and IOs.

We have implemented the scheme into the extended LAPW method and studied both the accuracy of the representation of the dielectric function and the intrinsic accuracy of the underlying wave functions.

We have applied the new method to the dielectric function of cubic *sp* metals Al, Li, Na, K, Rb, and Cs with the aim to understand what can be learned from the anisotropy of their bulk loss function. In the non-free-electron-like metals Li, K, Rb, and Cs the anisotropy of the plasmon dispersion is rather irregular due to the vicinity of the intra- and interband transitions to the plasmon. In contrast, in Al and Na, the plasmon occurs well above the intense interband transitions, and their effect is much tinier. We have reproduced the sign and the qualitative trend of the $\mathbf{q}$ dependence of the anisotropy in both metals, although the absolute values are substantially overestimated in the calculation. We revealed a strong similarity of the structure of the particle-hole transitions in Al and Na and traced the plasmon anisotropy to the energy location of the plasmon relative to very subtle features of the imaginary DF, which are barely visible in the $\epsilon_2(\omega)$ spectrum. Our analysis demonstrates that the electron energy loss spectroscopy experiment is sensitive to subtle details of the unoccupied bulk band structure and may give access to features not reachable with angle-integrated (optics) or surface-sensitive electron spectroscopies.

ACKNOWLEDGMENTS

We thank P. Koval, R. Kuzian, V. Nazarov, I. Nechaev, and V. Silkin for enlightening discussions. This work was supported by the Spanish Ministry of Economy, Industry and Competitiveness MINEICO (Project No. FIS2016-76617-P) and by the Departamento de Educación, Política Lingüística y Cultura of the Basque government (Project No. PI2017-30).

APPENDIX A: ACCURACY AND CONVERGENCE

Let us study the properties of the product basis set regarding the plane-wave cutoff of ψ^{F} and the angular-momentum cutoff of ψ^{I}, see Eq. (4). We first consider the momentum operator $\hat{\mathbf{p}} = -i\hbar\nabla$, which is related to the $q \to 0$ limit of the operator $\exp(i\mathbf{q}\cdot\mathbf{r})/q$; see Eq. (13). This will give the idea of the accuracy of the filtered wave functions because the operator $\hat{\mathbf{p}}$ itself is treated exactly, and the result can be compared with the exact value calculated from the complete APW representation of the wave function. To have an idea of the accuracy of the momentum matrix elements (MMEs), let us consider its $\mathbf{k}$-averaged value, which we define as the ratio of the absorption probability

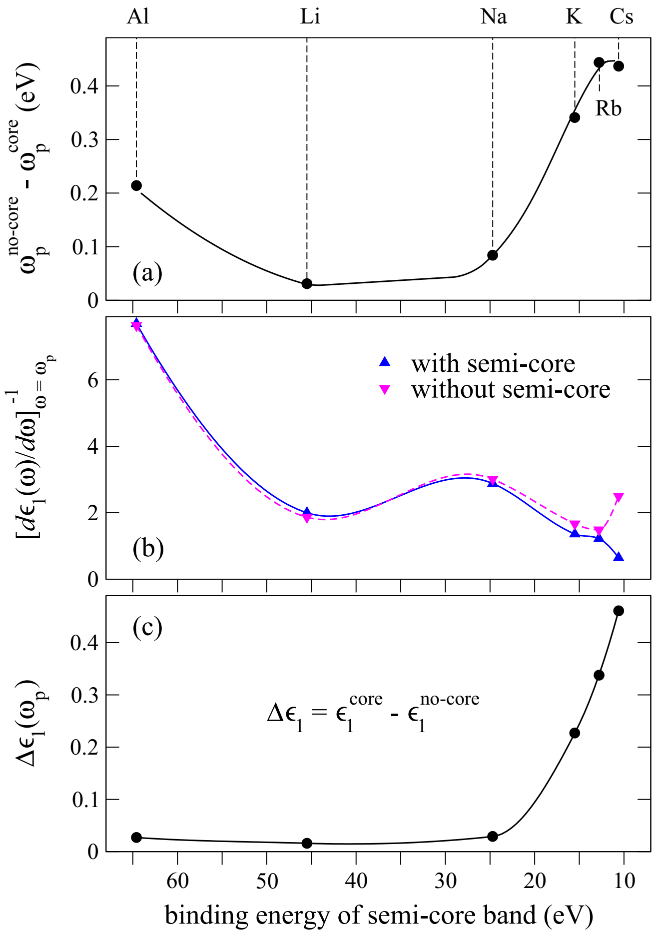

FIG. 9. Effect of the semi-core excitations on the plasmon energy for Al, Li, Na, K, Rb, and Cs for $\mathbf{q} = 0$. (a) Dependence of the plasmon energy shift due to the semi-core excitations on the binding energy of the semi-core band. (b) Plasmon sensitivity $[d\epsilon_1(\omega)/d\omega]^{-1}$. (c) Semi-core contribution to $\epsilon_1(\omega_{\mathrm{p}})$.

$$W(\omega) = \sum_{mn} \int_{\mathrm{BZ}} d\mathbf{k} P_{mn}^{\mathbf{k}} \delta\left(E_n^{\mathbf{k}} - E_m^{\mathbf{k}} - \hbar\omega\right) \tag{A1}$$

to the joint density of states $J(\omega)$, which is obtained by setting the transition probability $P_{mn}^{\mathbf{k}}$ in Eq. (A1) to unity,

$$R(\omega) = W(\omega)/J(\omega). \tag{A2}$$

The sum in Eq. (A1) runs over all occupied states $|n\mathbf{k}\rangle$ and unoccupied states $|m\mathbf{k}\rangle$. For a cubic crystal the dipole transition probability is $P_{mn}^{\mathbf{k}} = \frac{1}{3}|\langle m\mathbf{k}|\hat{\mathbf{p}}|n\mathbf{k}\rangle|^2$.

It follows from the dipole selection rules that, for reasonably small values of S_γ, the $l_{\max}$ cutoff in Eq. (8) does not need to exceed the highest angular momentum of the atomic valence shell plus one. This is illustrated for Cs in Figs. 7(a) and 7(b) and for Cu in Figs. 7(c) and 7(d). Surprisingly, for Cs, not only for a moderate $S_\gamma = 3$ a.u. but also for a very large $S_\gamma = 5$ a.u. at $l_{\max} = 2$ the error is negligible. Note that the results with the smaller S_γ are slightly more accurate although a larger part of the wave function is described by plane waves. While for Cs the challenging aspect is the angular-momentum expansion of ψ^{I} in a large sphere, for Cu it is the plane-wave expansion of ψ^{F}. Figures 7(e) and 7(f) show the PW-convergence of the momentum matrix elements (MMEs) for $S_\gamma = 1.2$ and 2.4 a.u., respectively. Note that, for $S_\gamma = 2.4$ a.u., which is close to the MT radius, $R(\omega)$ converges already at 89 PWs, which equals the number of APWs needed to obtain the band structure. The obvious advantage of the new basis is that PWs are orthogonal and the momentum operator is diagonal.

For the operator $\exp(i\mathbf{q}\cdot\mathbf{r})$ there arises the question of the convergence of its Rayleigh expansion, i.e., of the sum over l'' in Eq. (8). The convergence of the $\mathbf{k}$-averaged matrix element $|\langle m\mathbf{k}+\mathbf{q}|\exp(i\mathbf{q}\cdot\mathbf{r})|n\mathbf{k}\rangle|^2$ is illustrated in Fig. 8 for Cs for $S_\gamma = 3$ and 5 a.u. The role of quadrupole transitions is seen to increase with q, especially for the larger S_γ. Interestingly, the quadrupole transitions from the semi-core $5p$ states are more intense than from the valence band. Figure 8 demonstrates that the l'' convergence can be accelerated by diminishing the γ sphere.

APPENDIX B: EFFECT OF SEMI-CORE STATES

The effect of the polarization of localized atomic-like states on the plasmon energy was considered by Lee and Chang [49] for Al and by Fleszar, Stumpf, and Eguiluz [41] for Cs. The results of the present work are shown in Fig. 9. The effect is seen to diminish monotonically over the series from Cs to Li as a function of the binding energy, but it grows again for Al; see Fig. 9(a). The reason for this is the higher sensitivity of the plasmon energy in Al; see Fig. 9(b) and a higher (relative to Li and Na) intensity of the semi-core transitions due to the stronger atomic potential; Fig. 9(c). Our data qualitatively agree with the estimate of Ref. [49] for Al, $\Delta\omega_{\mathrm{p}} = 0.35$ eV, and of Ref. [41] for Cs, $\Delta\omega_{\mathrm{p}} = 0.5$ eV (both estimated from experimental data).

[1] G. Giuliani and G. Vignale, *Quantum Theory of the Electron Liquid*, Masters Series in Physics and Astronomy (Cambridge University Press, Cambridge, 2005).

[2] L. Hedin, New method for calculating the one-particle Green's function with application to the electron-gas problem, Phys. Rev. **139**, A796 (1965).

[3] F. Aryasetiawan and O. Gunnarsson, The GW method, Rep. Prog. Phys. **61**, 237 (1998).

[4] H. Haug and S. Koch, *Quantum Theory of the Optical and Electronic Properties of Semiconductors* (World Scientific, Singapore, 2004).

[5] D. Pines, *Elementary Excitations in Solids*, Lecture Notes and Supplements in Physics (Benjamin, New York, 1963).

[6] P. J. Feibelman, Surface electromagnetic fields, Prog. Surf. Sci. **12**, 287 (1982).

[7] A. Liebsch, *Electronic Excitations at Metal Surfaces* (Plenum, New York, 1997).

[8] J. M. Pitarke, V. M. Silkin, E. V. Chulkov, and P. M. Echenique, Theory of surface plasmons and surface-plasmon polaritons, Rep. Prog. Phys. **70**, 1 (2007).

[9] E. E. Krasovskii, V. M. Silkin, V. U. Nazarov, P. M. Echenique, and E. V. Chulkov, Dielectric screening and band-structure effects in low-energy photoemission, Phys. Rev. B **82**, 125102 (2010).

[10] F. Siek, S. Neb, P. Bartz, M. Hensen, C. Strüber, S. Fiechter, M. Torrent-Sucarrat, V. Silkin, E. Krasovskii, N. Kabachnik, S. Fritzsche, R. Muiño, P. Echenique, A. Kazansky, N. Müller, W. Pfeiffer, and U. Heinzmann, Angular momentum-induced delays in solid-state photoemission enhanced by intra-atomic interactions, Science **357**, 1274 (2017).

[11] V. U. Nazarov, V. M. Silkin, and E. E. Krasovskii, Probing mesoscopic crystals with electrons: One-step simultaneous inelastic and elastic scattering theory, Phys. Rev. B **96**, 235414 (2017).

[12] J. E. Harriman, Densities, operators, and basis sets, Phys. Rev. A **34**, 29 (1986).

[13] M. C. Payne, M. P. Teter, D. C. Allan, T. A. Arias, and J. D. Joannopoulos, Iterative minimization techniques for *ab initio* total-energy calculations: Molecular dynamics and conjugate gradients, Rev. Mod. Phys. **64**, 1045 (1992).

[14] P. E. Blöchl, Projector augmented-wave method, Phys. Rev. B **50**, 17953 (1994).

[15] S. Brodersen, D. Lukas, and W. Schattke, Calculation of the dielectric function in a local representation, Phys. Rev. B **66**, 085111 (2002).

[16] J. J. Mortensen, L. B. Hansen, and K. W. Jacobsen, Real-space grid implementation of the projector augmented wave method, Phys. Rev. B **71**, 035109 (2005).

[17] J. Yan, J. J. Mortensen, K. W. Jacobsen, and K. S. Thygesen, Linear density response function in the projector augmented wave method: Applications to solids, surfaces, and interfaces, Phys. Rev. B **83**, 245122 (2011).

[18] X. Blase and P. Ordejón, Dynamical screening and absorption within a strictly localized basis implementation of time-dependent LDA: From small clusters and molecules to azafullerenes, Phys. Rev. B **69**, 085111 (2004).

[19] P. Umari, G. Stenuit, and S. Baroni, Optimal representation of the polarization propagator for large-scale *GW* calculations, Phys. Rev. B **79**, 201104(R) (2009).

[20] F. Aryasetiawan and O. Gunnarsson, Product-basis method for calculating dielectric matrices, Phys. Rev. B **49**, 16214 (1994).

[21] D. Foerster, Elimination, in electronic structure calculations, of redundant orbital products, J. Chem. Phys. **128**, 034108 (2008).

[22] J. C. Slater, Wave functions in a periodic potential, Phys. Rev. **51**, 846 (1937).

[23] O. K. Andersen, Linear methods in band theory, Phys. Rev. B **12**, 3060 (1975).

[24] D. D. Koelling and G. O. Arbman, Use of energy derivative of the radial solution in an augmented plane wave method: Application to copper, J. Phys. F: Met. Phys. **5**, 2041 (1975).

[25] D. Singh, Ground-state properties of lanthanum: Treatment of extended-core states, Phys. Rev. B **43**, 6388 (1991).

[26] E. E. Krasovskii, Accuracy and convergence properties of the extended linear augmented-plane-wave method, Phys. Rev. B **56**, 12866 (1997).

[27] H. Jiang, R. I. Gómez-Abal, X.-Z. Li, C. Meisenbichler, C. Ambrosch-Draxl, and M. Scheffler, FHI-gap: A *GW* code based on the all-electron augmented plane wave method, Comput. Phys. Commun. **184**, 348 (2013).

[28] C. Friedrich, S. Blügel, and A. Schindlmayr, Efficient implementation of the *GW* approximation within the all-electron FLAPW method, Phys. Rev. B **81**, 125102 (2010).

[29] D. Nabok, A. Gulans, and C. Draxl, Accurate all-electron G_0W_0 quasiparticle energies employing the full-potential augmented plane-wave method, Phys. Rev. B **94**, 035118 (2016).

[30] T. Kotani and M. van Schilfgaarde, All-electron GW approximation with the mixed basis expansion based on the full-potential LMTO method, Solid State Commun. **121**, 461 (2002).

[31] C. Friedrich, M. C. Müller, and S. Blügel, Band convergence and linearization error correction of all-electron *GW* calculations: The extreme case of zinc oxide, Phys. Rev. B **83**, 081101(R) (2011).

[32] E.-N. Foo and J. J. Hopfield, Optical absorption and energy loss in sodium in the Hartree approximation, Phys. Rev. **173**, 635 (1968).

[33] E. E. Krasovskii and W. Schattke, Semirelativistic technique for $\mathbf{k} \cdot \mathbf{p}$ calculations: Optical properties of Pd and Pt, Phys. Rev. B **63**, 235112 (2001).

[34] G. Michalicek, M. Betzinger, C. Friedrich, and S. Blügel, Elimination of the linearization error and improved basis-set convergence within the FLAPW method, Comput. Phys. Commun. **184**, 2670 (2013).

[35] E. E. Krasovskii, F. Starrost, and W. Schattke, Augmented fourier components method for constructing the crystal potential in self-consistent band-structure calculations, Phys. Rev. B **59**, 10504 (1999).

[36] E. E. Krasovskii and W. Schattke, Local field effects in optical excitations of semicore electrons, Phys. Rev. B **60**, R16251 (1999).

[37] M. Betzinger, C. Friedrich, S. Blügel, and A. Görling, Local exact exchange potentials within the all-electron FLAPW method and a comparison with pseudopotential results, Phys. Rev. B **83**, 045105 (2011).

[38] P. Koval, D. Foerster, and D. Sánchez-Portal, Fully self-consistent *GW* and quasiparticle self-consistent *GW* for molecules, Phys. Rev. B **89**, 155417 (2014).

[39] H. Jiang, Revisiting the *GW* approach to d- and f-electron oxides, Phys. Rev. B **97**, 245132 (2018).

[40] F. Aryasetiawan and K. Karlsson, Energy Loss Spectra and Plasmon Dispersions in Alkali Metals: Negative Plasmon Dispersion in Cs, Phys. Rev. Lett. **73**, 1679 (1994).

[41] A. Fleszar, R. Stumpf, and A. G. Eguiluz, One-electron excitations, correlation effects, and the plasmon in cesium metal, Phys. Rev. B **55**, 2068 (1997).

[42] M. Cazzaniga, H.-C. Weissker, S. Huotari, T. Pylkkänen, P. Salvestrini, G. Monaco, G. Onida, and L. Reining, Dynamical response function in sodium and aluminum from time-dependent density-functional theory, Phys. Rev. B **84**, 075109 (2011).

[43] H. Ehrenreich and M. H. Cohen, Self-consistent field approach to the many-electron problem, Phys. Rev. **115**, 786 (1959).

[44] G. Lehmann and M. Taut, On the numerical calculation of the density of states and related properties, Phys. Status Solidi B **54**, 469 (1972).

[45] K. Utsumi and S. Ichimaru, Dielectric formulation of strongly coupled electron liquids at metallic densities. VI. Analytic expression for the local-field correction, Phys. Rev. A **26**, 603 (1982).

[46] J. Sprösser-Prou, A. vom Felde, and J. Fink, Aluminum bulk-plasmon dispersion and its anisotropy, Phys. Rev. B **40**, 5799 (1989).

[47] A. vom Felde, J. Sprösser-Prou, and J. Fink, Valence-electron excitations in the alkali metals, Phys. Rev. B **40**, 10181 (1989).

[48] C. H. Chen and J. Silcox, Direct nonvertical interband transitions at large wave vectors in aluminum, Phys. Rev. B **16**, 4246 (1977).

[49] K.-H. Lee and K. J. Chang, First-principles study of the optical properties and the dielectric response of Al, Phys. Rev. B **49**, 2362 (1994).

[50] J. Lindhard, On the properties of a gas of charged particles, K. Dan. Vidensk. Selsk. Mat.-Fys. Medd. **28**, 1 (1954).

[51] H. Bross, Pseudopotential theory of the dielectric function of Al-the volume plasmon dispersion, J. Phys. F: Met. Phys. **8**, 2631 (1978).

[52] K. Sturm and L. E. Oliveira, Theory of a zone-boundary collective state in Al: A model calculation, Phys. Rev. B **30**, 4351 (1984).

[53] K. Sturm and L. E. Oliveira, Zone boundary collective states in lithium and sodium, Europhys. Lett. **9**, 257 (1989).

[54] N. E. Maddocks, R. W. Godby, and R. J. Needs, Bandstructure effects in the dynamic response of aluminium, Europhys. Lett. **27**, 681 (1994).

[55] S. Kaltenborn and H. C. Schneider, Plasmon dispersions in simple metals and Heusler compounds, Phys. Rev. B **88**, 045124 (2013).

[56] M. Taut and K. Sturm, Plasmon dispersion constant of the alkali metals, Solid State Commun. **82**, 295 (1992).

[57] A. A. Quong and A. G. Eguiluz, First-Principles Evaluation of Dynamical Response and Plasmon Dispersion in Metals, Phys. Rev. Lett. **70**, 3955 (1993).

[58] W. Ku and A. G. Eguiluz, Plasmon Lifetime in K: A Case Study of Correlated Electrons in Solids Amenable to *Ab Initio* Theory, Phys. Rev. Lett. **82**, 2350 (1999).

[59] S. Huotari, C. Sternemann, M. C. Troparevsky, A. G. Eguiluz, M. Volmer, H. Sternemann, H. Müller, G. Monaco, and W. Schülke, Strong deviations from jellium behavior in the valence electron dynamics of potassium, Phys. Rev. B **80**, 155107 (2009).

[60] V. M. Silkin, A. Rodriguez-Prieto, A. Bergara, E. V. Chulkov, and P. M. Echenique, Strong variation of dielectric response and optical properties of lithium under pressure, Phys. Rev. B **75**, 172102 (2007).

[61] A. Rodriguez-Prieto, V. M. Silkin, A. Bergara, and P. M. Echenique, Energy loss spectra of lithium under pressure, New J. Phys. **10**, 053035 (2008).

[62] I. Errea, A. Rodriguez-Prieto, B. Rousseau, V. M. Silkin, and A. Bergara, Electronic collective excitations in compressed lithium from *ab initio* calculations: Importance and anisotropy of local-field effects at large momenta, Phys. Rev. B **81**, 205105 (2010).

[63] I. Loa, K. Syassen, G. Monaco, G. Vankó, M. Krisch, and M. Hanfland, Plasmons in Sodium Under Pressure: Increasing Departure from Nearly Free-Electron Behavior, Phys. Rev. Lett. **107**, 086402 (2011).

[64] M. Attarian Shandiz and R. Gauvin, Density functional and theoretical study of the temperature and pressure dependency of the plasmon energy of solids, J. Appl. Phys. **116**, 163501 (2014).

[65] J. Ibañez-Azpiroz, B. Rousseau, A. Eiguren, and A. Bergara, *Ab initio* analysis of plasmon dispersion in sodium under pressure, Phys. Rev. B **89**, 085102 (2014).

[66] Z. Yu, H. Y. Geng, Y. Sun, and Y. Chen, Optical properties of dense lithium in electride phases by first-principles calculations, Sci. Rep. **8**, 3868 (2018).

[67] M. Taut, Exchange-correlation correction to the dielectric function of the inhomogeneous electron gas, J. Phys.: Condens. Matter **4**, 9595 (1992).

[68] K. Karlsson and F. Aryasetiawan, Plasmon lifetime, zone-boundary collective states, and energy-loss spectra of lithium, Phys. Rev. B **52**, 4823 (1995).

[69] I. A. Nechaev, V. M. Silkin, and E. V. Chulkov, Inclusion of the exchange-correlation effects in *ab initio* methods for calculating the plasmon dispersion and line width in metals, Phys. Solid State **49**, 1820 (2007).

[70] M. Urner-Wille and H. Raether, Anisotropy of the 15 eV volume plasmon dispersion in A1, Phys. Lett. A **58**, 265 (1976).

[71] E. Petri, A. Otto, and W. Hanke, Anisotropy of plasmon dispersion in Al: An electron correlation effect, Solid State Commun. **19**, 711 (1976).

[72] W. Schülke, H. Nagasawa, S. Mourikis, and P. Lanzki, Dynamic structure of electrons in Li metal: Inelastic synchrotron x-ray scattering results and interpretation beyond the random-phase approximation, Phys. Rev. B **33**, 6744 (1986).

[73] K. Sturm, Band structure effects on the plasmon dispersion in simple metals, Z. Phys. B: Condens. Matter Quanta **29**, 27 (1978).

[74] W. Schülke, H. Nagasawa, and S. Mourikis, Dynamic Structure Factor of Electrons in Li by Inelastic Synchrotron X-Ray Scattering, Phys. Rev. Lett. **52**, 2065 (1984).